

ADVANCED MATERIALS

Supporting Information

for *Adv. Mater.*, DOI: 10.1002/adma.201605198

Gigahertz Electromagnetic Structures via Direct Ink Writing
for Radio-Frequency Oscillator and Transmitter Applications

Nanjia Zhou, Chengye Liu, Jennifer A. Lewis, and Donhee
Ham**

DOI: 10.1002/adma.201605198

Article type: Communication

Supporting Information

Gigahertz Electromagnetic Structures via Direct Ink Writing for Radio-Frequency Oscillator and Transmitter Applications

Nanjia Zhou, Chengye Liu, Jennifer A. Lewis, and Donhee Ham**

Dr. N. Zhou,^[+] Prof. J. A. Lewis
Wyss Institute for Biologically Inspired Engineering
John A. Paulson School of Engineering and Applied Sciences
Harvard University
Cambridge, MA 02138, USA

E-mail: jalewis@seas.harvard.edu

C. Liu,^[+] Prof. D. Ham
John A. Paulson School of Engineering and Applied Sciences
Harvard University
Cambridge, MA 02138, USA
E-mail: donhee@seas.harvard.edu

^[+]These authors contributed equally to this work.

Keywords: electronics, wireless, 3D printing, silver ink

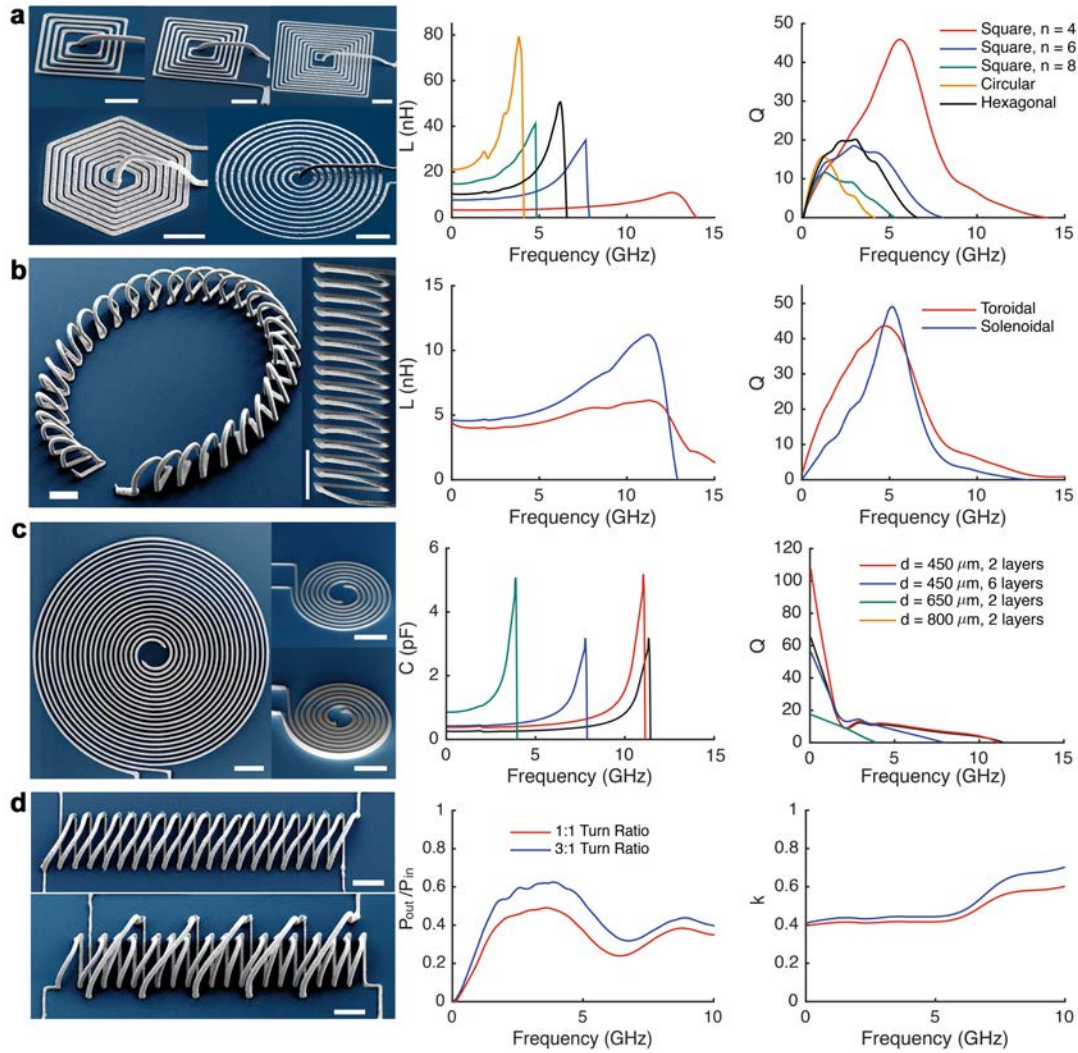


Figure S1. Lumped passives printed on glass substrates and their measured RF characteristics (printed devices shown in Figure 1b,c are also included). a) Planar spiral inductors of square (metal width w : ≈ 10 μm , metal thickness t : 6-8 μm , metal-metal spacing s : ≈ 10 μm , side length of the outermost turn l_{out} : 240, 320, and 400 μm for number of turns n of 4, 6, and 8), hexagonal (w : ≈ 10 μm , t : 6-8 μm , s : ≈ 2 μm , l_{out} : 200 μm , n : 9), and circular (w : ≈ 10 μm , t : 6-8 μm , s : ≈ 14 μm , outer diameter d : 590 μm , n : 10) shapes. b) Toroidal (w : ≈ 10 μm , t : ≈ 10 μm , cross-sectional turn radius r : ≈ 50 μm , n : 33) and solenoidal (w : ≈ 10 μm , t : ≈ 10 μm , s : ≈ 22 μm , r : ≈ 100 μm , n : 16) inductors. c) Parallel-plate capacitors (w : ≈ 10 μm , t : 12-36 μm , s : 7-10 μm , d : 450, 650, and 800 μm). d) 1:1 and 3:1 transformers. 1:1 transformer: w : ≈ 10 μm , t : ≈ 10 μm , s for each winding: ≈ 90 μm , r : ≈ 100 μm . 3:1 transformer: w : ≈ 10 μm , t : ≈ 10 μm , primary winding s : 40-70 μm , primary winding r : ≈ 100 μm , secondary winding s : ≈ 170 μm , secondary winding r : ≈ 180 μm . All scale bars are 100 μm . Of note, the lumped LC resonator of Figure 1d consists of a toroidal inductor (w : ≈ 10 μm , t : ≈ 10 μm , r : ≈ 50 μm , n : 32) and a parallel-plate capacitor (w : ≈ 10 μm , t : ≈ 36 μm , s : ≈ 10 μm , d : 450 μm).

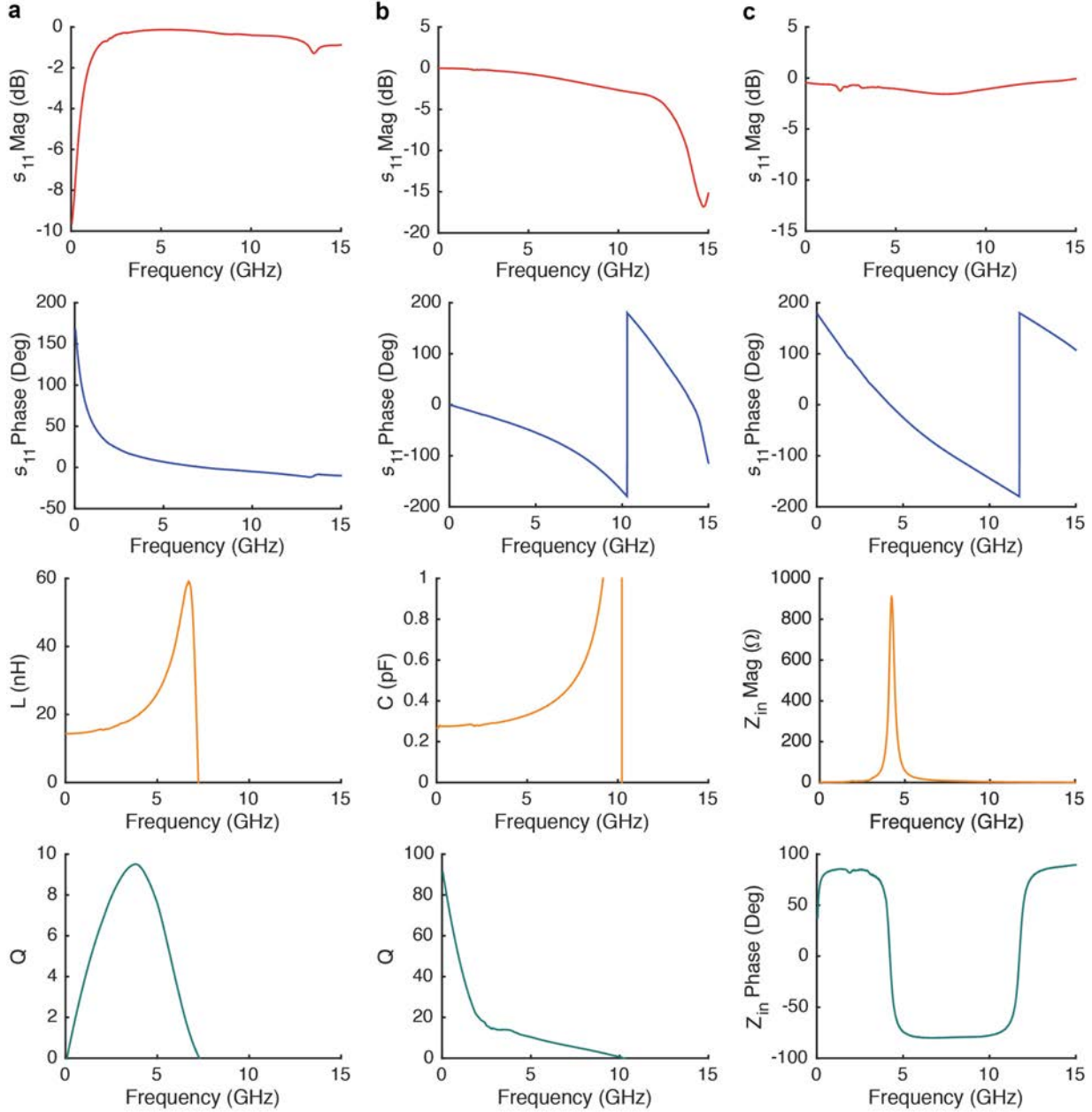


Figure S2. Measured s_{11} parameters and electrical parameters extracted from the s -parameters for three selected devices from Figure S1. a) the planar spiral inductor of square shape with w : ≈ 10 μm , t : 6-8 μm , s : ≈ 10 μm , l_{out} : 400 μm , n : 8. b) the capacitor with s : ≈ 7 μm , d : ≈ 450 μm , and t : ≈ 12 μm . c) the LC resonator consisting of toroidal inductor (w : ≈ 10 μm , t : ≈ 10 μm , r : ≈ 50 μm , n : 32) and a parallel-plate capacitor (w : ≈ 10 μm , t : ≈ 36 μm , s : ≈ 10 μm , d : 450 μm).

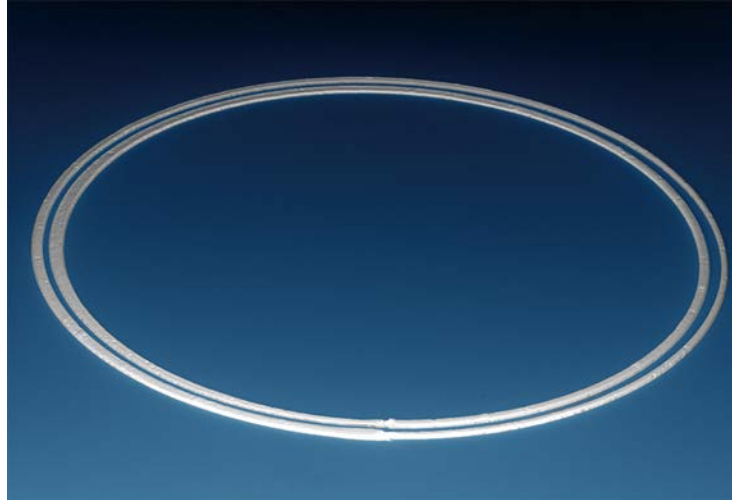


Figure S3. Simple CPS ring resonator printed on glass substrate. w : 50-80 μm , t : ≈ 30 μm , s : 30-70 μm , d : 5 mm. $|Z_{\text{in}}|$ of this simple CPS ring is shown in Figure 11, red.

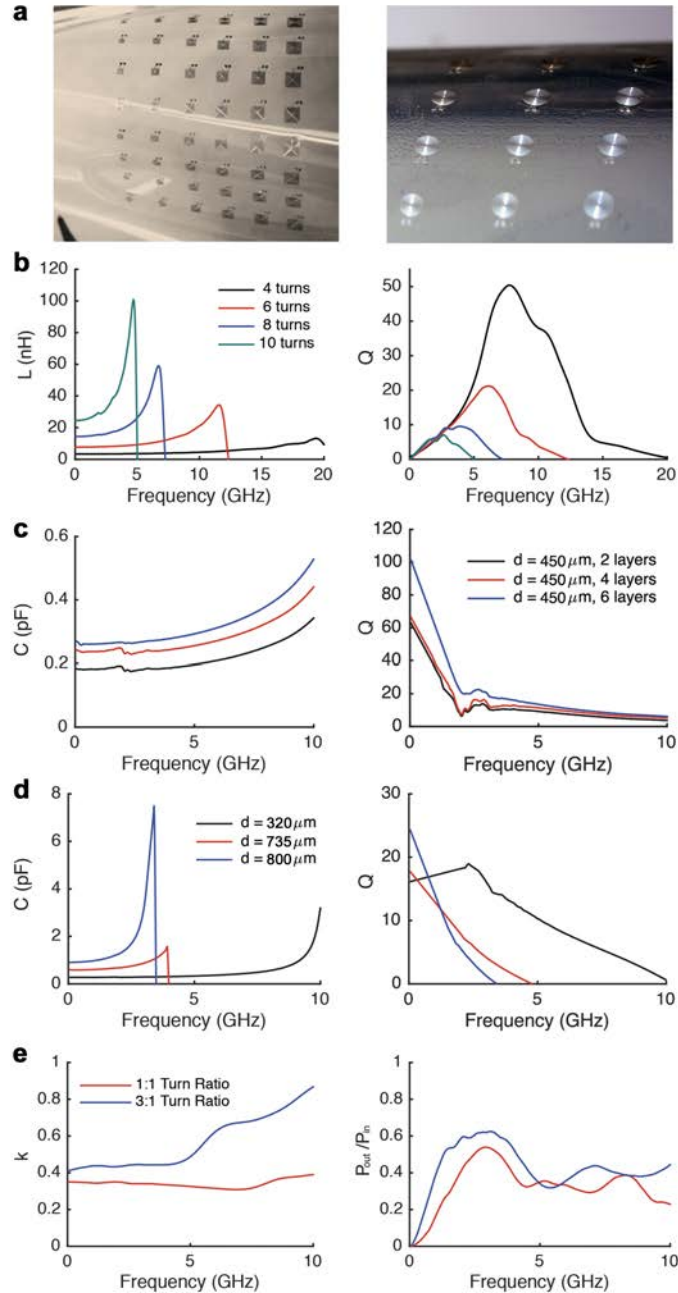


Figure S4. Lumped passives printed on flexible polyimide substrates and their measured RF characteristics. a) Planar square spiral inductors and parallel-plate capacitors. b) L and Q of the inductors (n : 4, 6, 8, and 10 with w , t , and s being the same as the square spiral inductors of Figure S1a). c) C and Q for the capacitors with s : $\approx 7 \mu\text{m}$, d : $\approx 450 \mu\text{m}$, and t : $\approx 12, 24$, and $36 \mu\text{m}$. d) C and Q for the capacitors with s : $\approx 7 \mu\text{m}$, d : $\approx 320, 735$, and $800 \mu\text{m}$, and t : $\approx 12 \mu\text{m}$. e) Coupling coefficients and power transfer efficiencies of 1:1 and 3:1 transformers with the same geometric parameters as the transformers of Figure S1d.

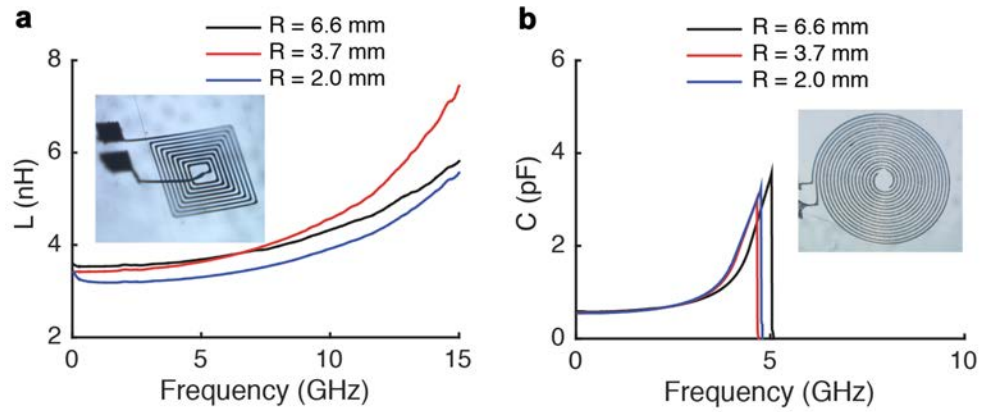


Figure S5. Bending test. a,b) Measured L and C for a planar square spiral inductor (n : 8 with w , t , and s being the same as the square spiral inductors of Figure S1a) and a parallel-plate capacitor (s : $\approx 7 \mu\text{m}$, d : $\approx 650 \mu\text{m}$, and t : $\approx 12 \mu\text{m}$) printed on flexible polyimide substrates with the substrates bent with bending radius, R , of 6.6, 3.7, and 2.0 mm.

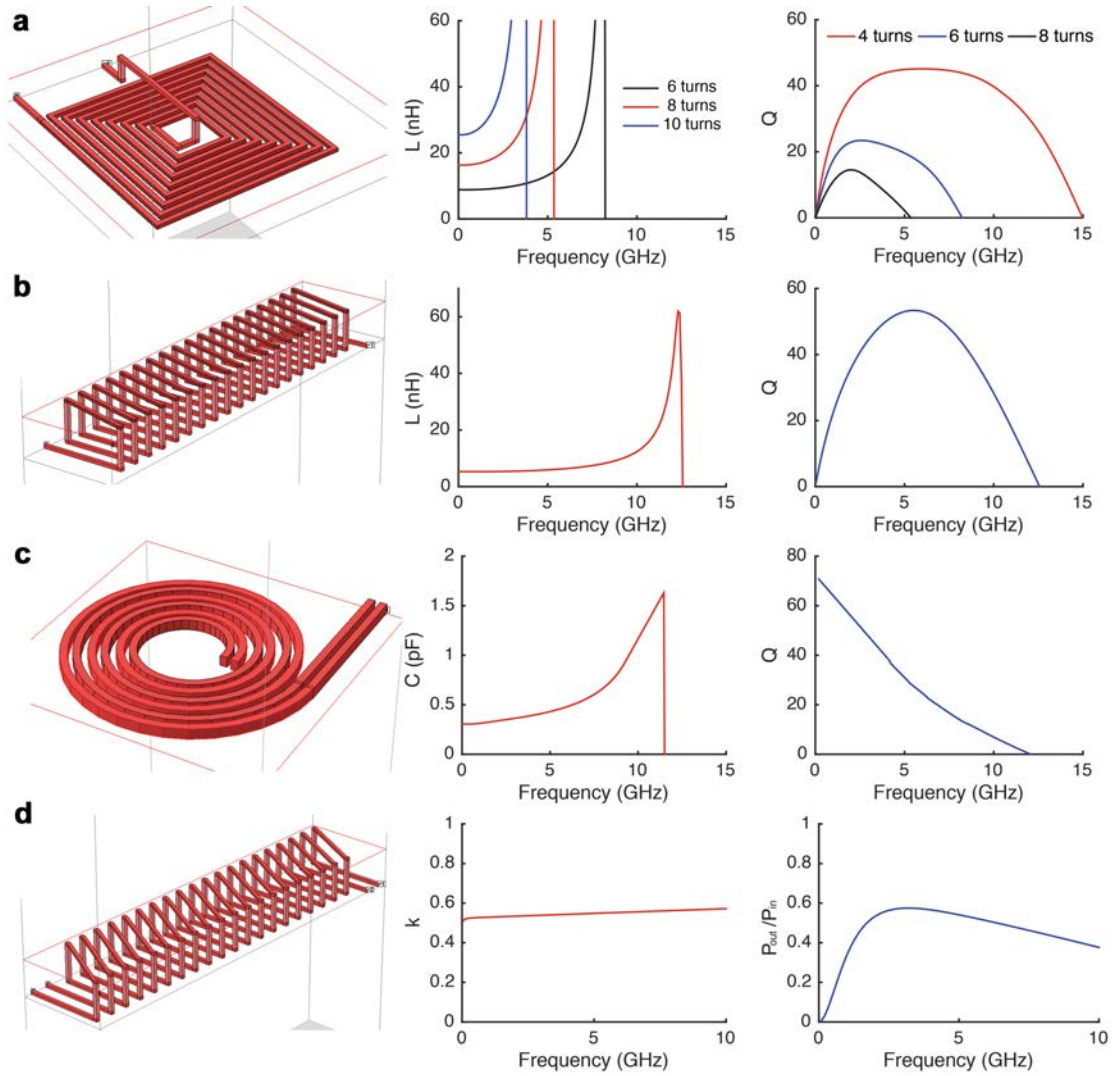


Figure S6. Representative electromagnetic simulation results for lumped passive structures. The electromagnetic field solver Sonnet outputs s -parameters, from which we extract circuit parameters using Equation S1-S7. a) Planar spiral inductors (w : $10\ \mu\text{m}$, t : $8\ \mu\text{m}$, s : $10\ \mu\text{m}$, l_{out} : 240 , 320 , and $400\ \mu\text{m}$ for n of 4 , 6 , and 8). b) Solenoidal inductor (w : $10\ \mu\text{m}$, t : $10\ \mu\text{m}$, turn dimensions: $200\ \mu\text{m} \times 100\ \mu\text{m}$, s : $50\ \mu\text{m}$, n : 19). c) Parallel-plate capacitor (w : $10\ \mu\text{m}$, t : $20\ \mu\text{m}$, s : $10\ \mu\text{m}$, d : $350\ \mu\text{m}$). d) 1:1 transformer (w : $10\ \mu\text{m}$, t : $10\ \mu\text{m}$, turn dimensions: $200\ \mu\text{m} \times 100\ \mu\text{m}$, s for each winding: $90\ \mu\text{m}$, n of each winding: 10). Due to the nature of the EM field solver, the circular turns of the implemented solenoidal inductor and transformer are approximated with rectangular turns in these simulations.

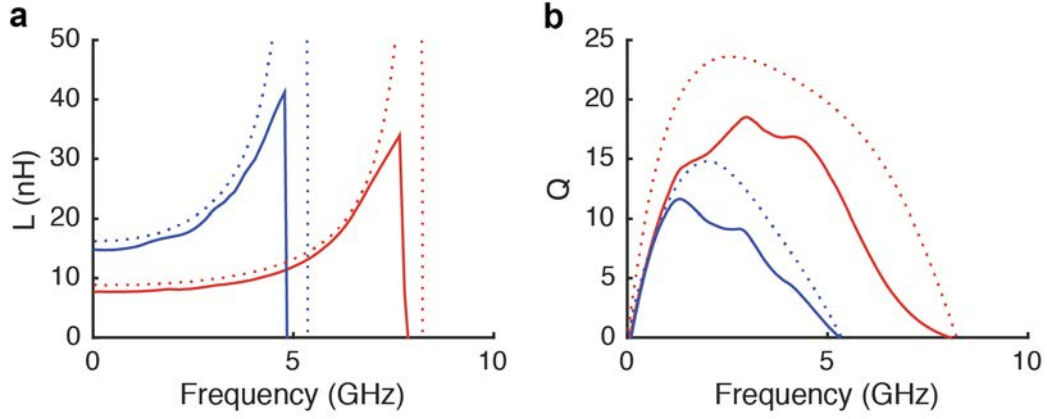


Figure S7. Comparison of measured (solid) and simulated (dashed) L and Q values for two planar square inductors. The red plots are for the planar square inductor with w : $\approx 10 \mu\text{m}$, t : 6-8 μm , s : $\approx 10 \mu\text{m}$, l_{out} : 320 μm , n : 6, and the blue plots are for the planar square inductor with w : $\approx 10 \mu\text{m}$, t : 6-8 μm , s : $\approx 10 \mu\text{m}$, l_{out} : 400 μm , n : 8. The measurement-simulation matches are overall good in all essential aspects, while the finite difference in details arises from the approximate resistance value used in simulation and also because the simulation does not take into account all parasitic elements.

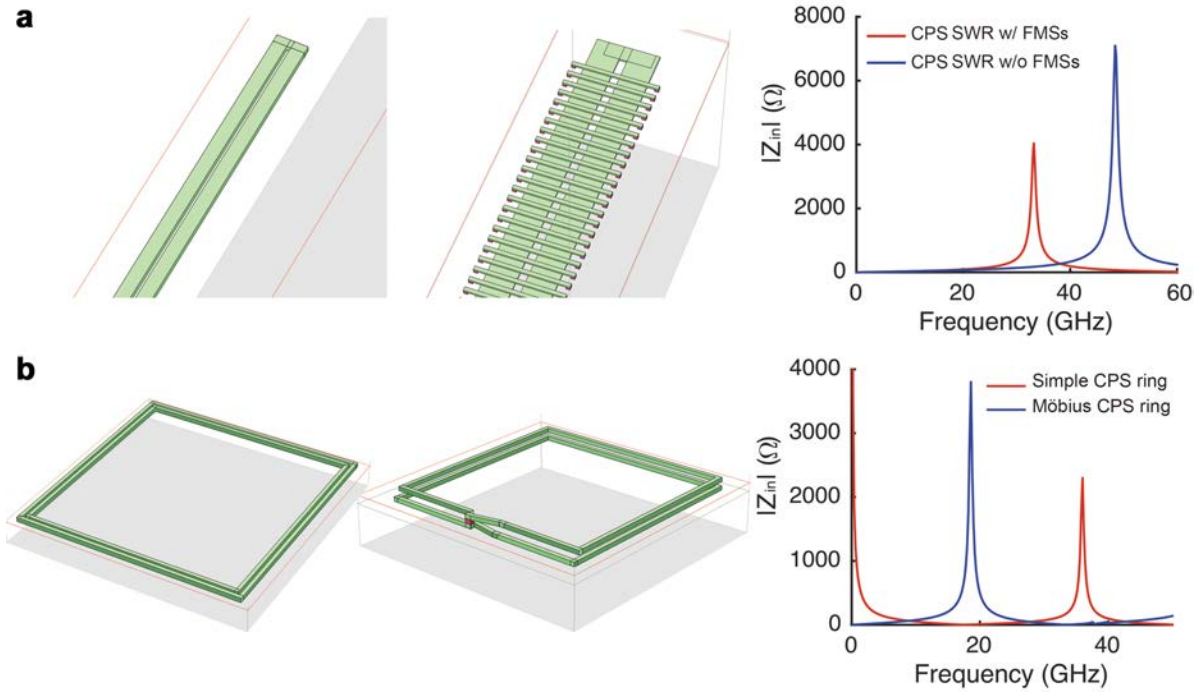


Figure S8. Representative electromagnetic simulation results for wave-based passive structures. a) CPS SWRs with and without FMSs (CPS l : 1 mm, w : 70 μm , t : 10 μm , s : 20 μm ; FMS l : 200 μm , w : 10 μm , t : 10 μm , s : 20 μm ; vertical spacing between CPS and FMS: 5 μm). b) CPS simple and Möbius rings (w : 30 μm , t : 30 μm , s : 30 μm , l_{out} : ≈ 1.5 mm); here we simulate square loops instead of circular loops due to the nature of the electromagnetic field solver, but this does not alter the basic operating principle of these resonant passive devices.

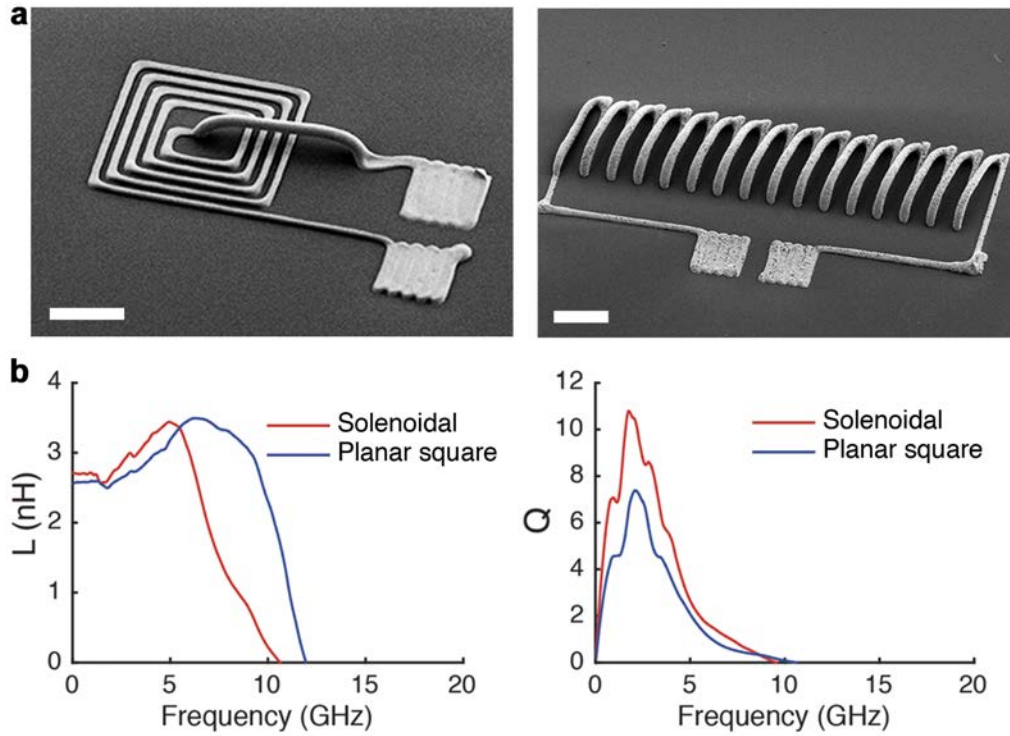


Figure S9. Inductors printed on silicon (conductive) substrate. Measured RF characteristics of a planar square inductor ($w: \approx 10 \mu\text{m}$, $t: \approx 8 \mu\text{m}$, $s: \approx 10 \mu\text{m}$, $l_{out}: 240$, $n: 4$), and a solenoidal inductor ($w: \approx 10 \mu\text{m}$, $t: \approx 10 \mu\text{m}$, $s: \approx 40 \mu\text{m}$, $r: \approx 100 \mu\text{m}$, $n: 16$) printed on silicon substrate used in standard CMOS processes. As the solenoidal inductor results in less eddy current loss in the conductive substrate than the planar inductor due to their magnetic field flux orientation difference, the solenoidal inductor exhibits a higher Q . Scale bars are $100 \mu\text{m}$.

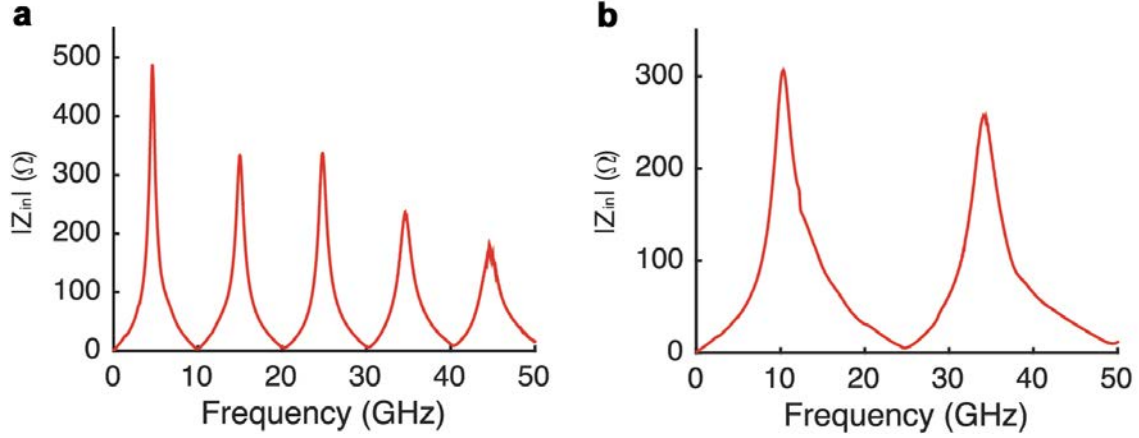


Figure S10. Harmonic analysis of CPS SWR data. a) Measured $|Z_{in}|$ of an FMS-free CPS SWR ($l = 13.4$ mm); this data is a replica of Figure 1j. $|Z_{in}|$ alternately exhibits local maxima and minima at frequencies of 4.6, 9.9, 15.0, 20.3, 24.8, 30.2, 34.6, 40.4, and 44.6 GHz. These correspond to the standing wave resonance modes, $l = n \times \lambda/4$ ($n = 1, 2, \dots, 9$). As shown in the table below, the measured harmonic frequency ratios follow ideal ratios well, while the ratio involving the first (fundamental) harmonic frequency shows a relatively larger deviation, because the fundamental tone is more heavily influenced by the non-idealities in the device and measurements.

Harmonic ratio	Measured	Ideal	Error (%)
f_2/f_1	2.15	$2/1 = 2.00$	7.61
f_3/f_2	1.52	$3/2 = 1.50$	1.01
f_4/f_3	1.35	$4/3 = 1.33$	1.50
f_5/f_4	1.22	$5/4 = 1.25$	-2.27
f_6/f_5	1.22	$6/5 = 1.20$	1.48
f_7/f_6	1.15	$7/6 = 1.17$	-1.80
f_8/f_7	1.17	$8/7 = 1.14$	2.17
f_9/f_8	1.10	$9/8 = 1.13$	-1.87

b) Measured $|Z_{in}|$ of an FMS-free CPS SWR ($l = 6.0$ mm); the data here is partially presented with the red curve of Figure 1k, but here the extended frequency range shows higher resonance modes as well. Once again $|Z_{in}|$ alternately exhibits local maxima and minima at 10.4, 24.7, 34.0, and 49.3 GHz, corresponding to the standing wave resonance modes, $l = n \times \lambda/4$ ($n = 1, 2, 3,$ and 4). As in the table below, the measured harmonic frequency ratios approximate ideal ratios reasonably well, with a relatively larger discrepancy involving the first harmonic frequency just like in (a).

Harmonic ratio	Measured	Ideal	Error (%)
f_2/f_1	2.38	$2/1 = 2.00$	18.75
f_3/f_2	1.38	$3/2 = 1.50$	-8.23
f_4/f_3	1.45	$4/3 = 1.33$	8.75

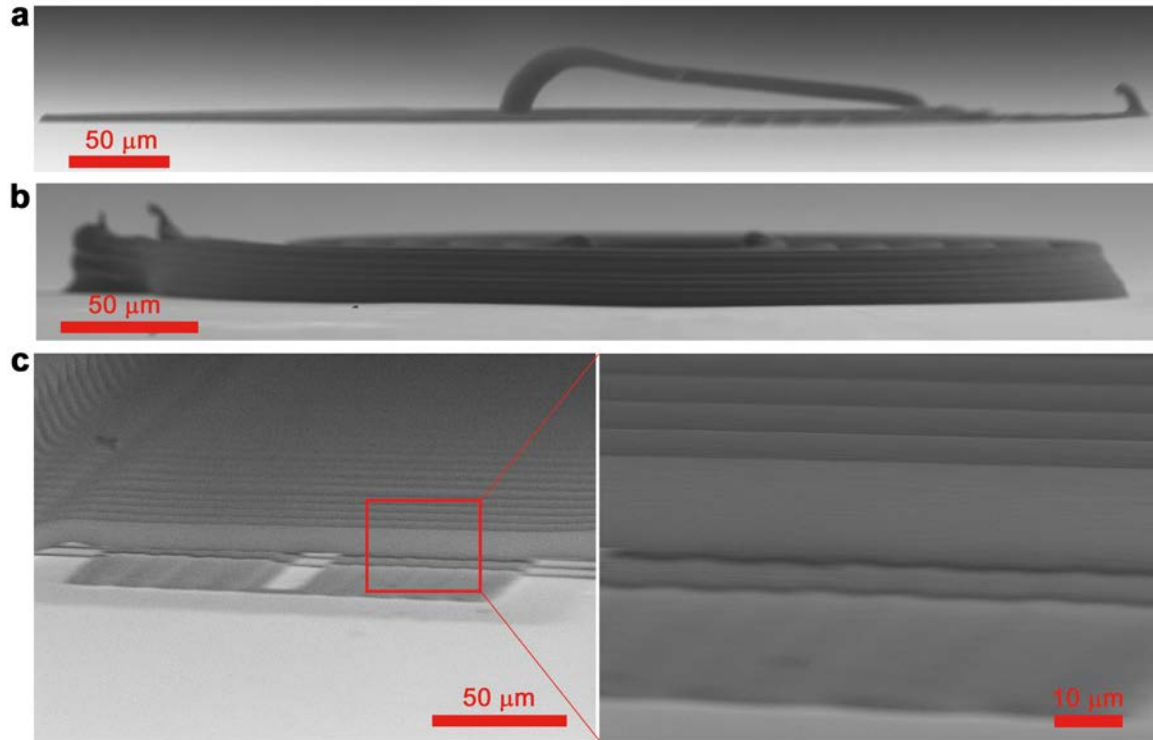


Figure S11. Scanning electron microscope (SEM) images of passives. a) The 6-turn inductor of Figure S1a. b) The $\approx 36 \mu\text{m}$ tall, $\approx 450 \mu\text{m}$ diameter capacitor of Figure S1c. c) The FMS-loaded CPS SWR of Figure 1e. Tilt angles are 89° , 88° , and 85° for (a), (b), and (c), respectively.

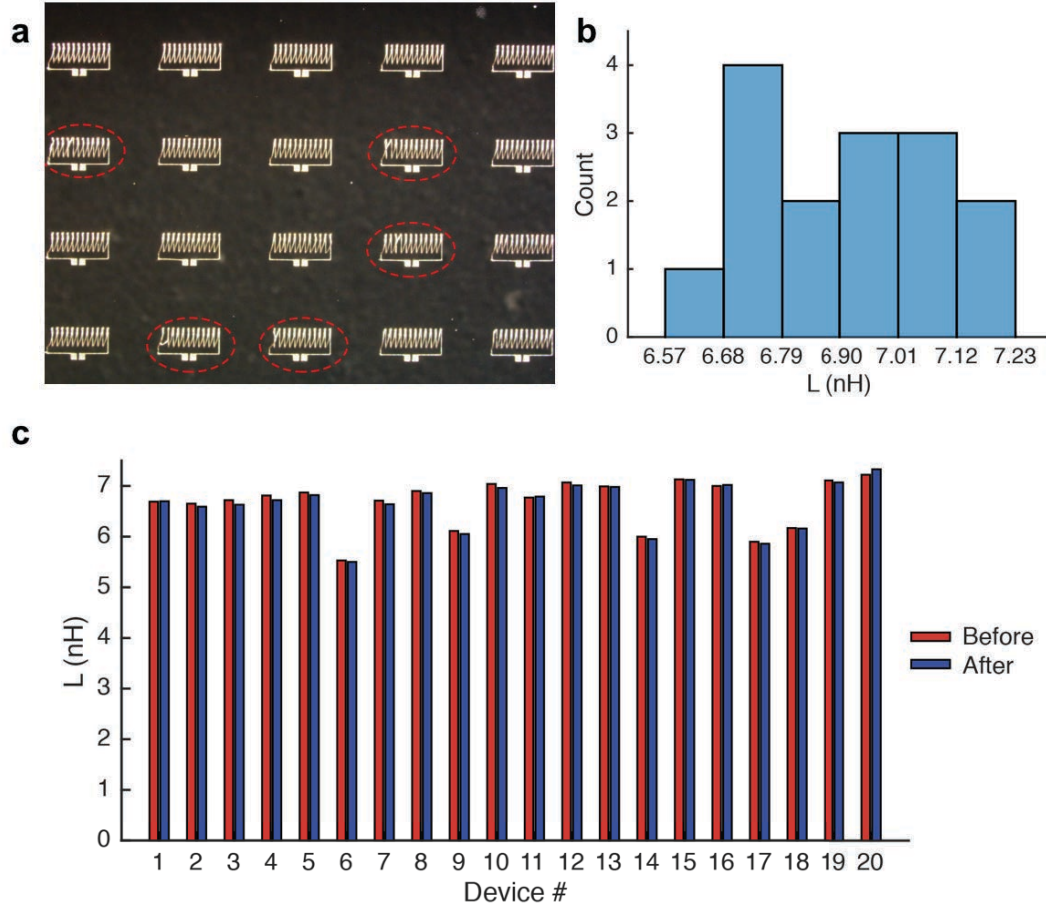


Figure S12. Yield and mechanical robustness: a) 20 solenoidal inductors printed in a single pass with intended identical design parameters of $w: \approx 10 \mu\text{m}$, $t: \approx 10 \mu\text{m}$, $s: \approx 60 \mu\text{m}$, $r: \approx 150 \mu\text{m}$, $n: 12$. In each of the 5 circled inductors, two adjacent turns are shorted during the printing process. b) For the remaining 15 inductors, measured 5-GHz inductance falls within $\pm 10\%$ of the target value 7 nH with an average inductance of 6.93 nH and a standard deviation of 0.164 nH. c) Measured 5-GHz inductance of all 20 solenoidal inductors before and after 12 h of a 3000 rpm rotation with an orbital diameter of $\approx 4.9 \text{ mm}$ (Note: Device #1 is located in the top, left corner, whereas Device #20 is located in the bottom, right corner of image (a)). The inductance changes only by an average of 0.48% after the mechanical perturbation. Note: The 5 defective inductors systematically exhibit smaller inductance values, since their shorted features effectively reduce the number of turns relative to other 15 (good) inductors.

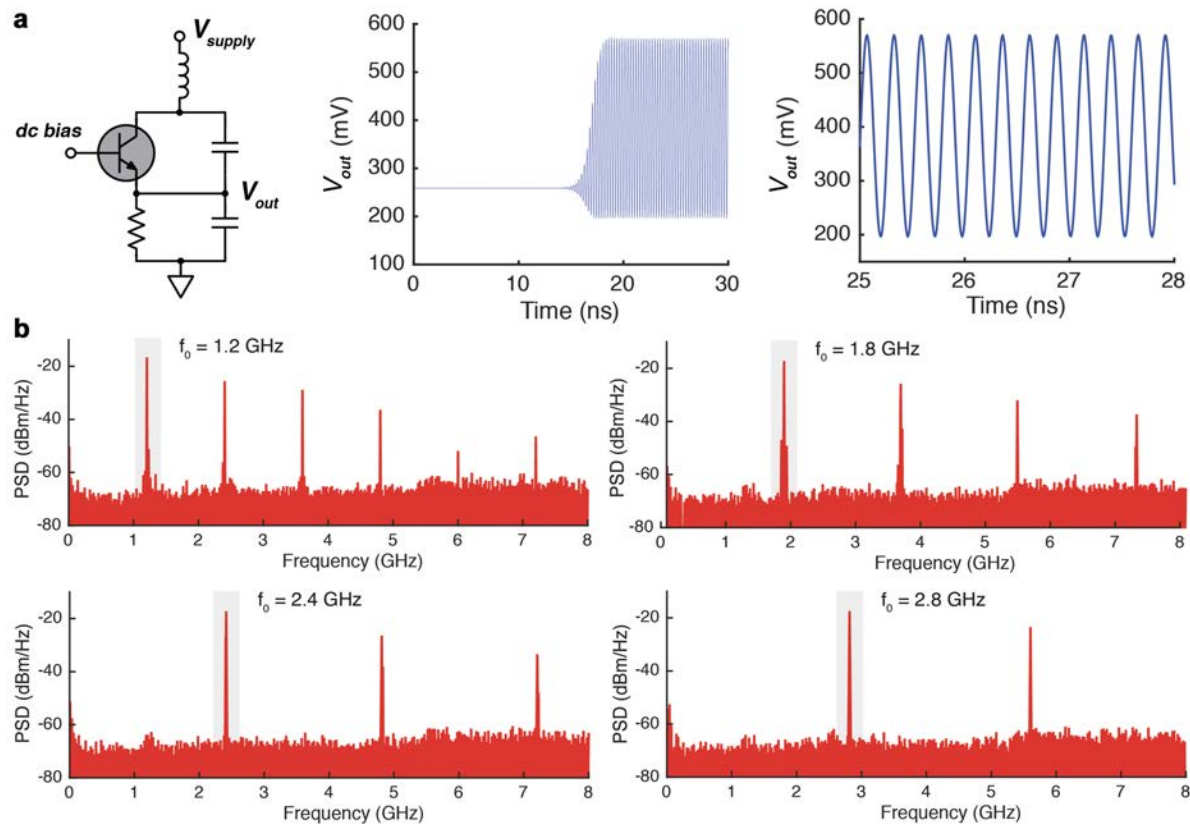


Figure S13. Simulation and measured frequency spectra of Colpitts LC oscillators. a) Circuit schematic and time-domain simulation showing the oscillation self-startup as well as its settlement into the steady-state oscillation. b) In addition to the 3.5 GHz Colpitts LC oscillator of Figure 2a, we build a number of other Colpitts LC oscillators on glass substrates with different oscillation frequencies. Measured power spectral densities (PSDs) of 4 such oscillators are shown here, with oscillation frequencies of 1.2, 1.8, 2.4, and 2.8 GHz.

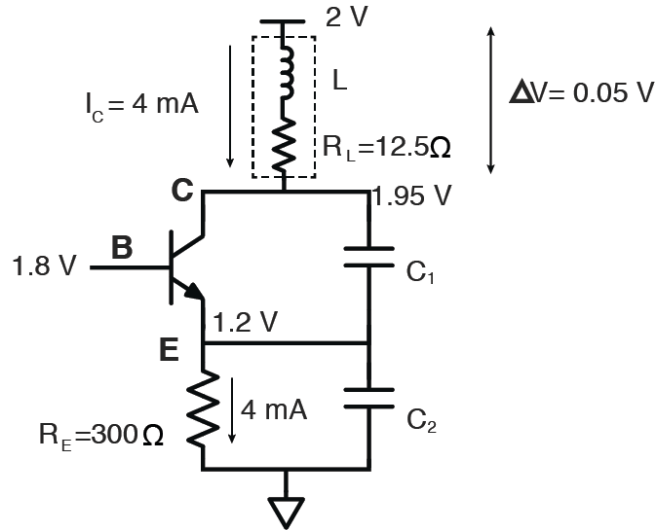


Figure S14. DC bias for the Colpitts oscillator shown in Figure 2. For the oscillator to start and self-sustain, the transistor must provide gain, and hence, it should be biased in the forward-active region at DC, that is, the base–emitter junction should be forward biased, and the base–collector junction should be reverse biased. This figure shows the DC bias voltage and current values in various nodes and paths, taking into account the DC voltage drop of 0.05 V across the printed inductor due to the parasitic resistance $R_L = 12.5 \Omega$ of the silver nanoparticle ink. From the calculated DC voltages of nodes, it is clear that the transistor is well into the forward-active region. In fact, the transistor will remain in the forward active bias until the DC voltage drop across the printed inductor becomes larger than 0.2 V.

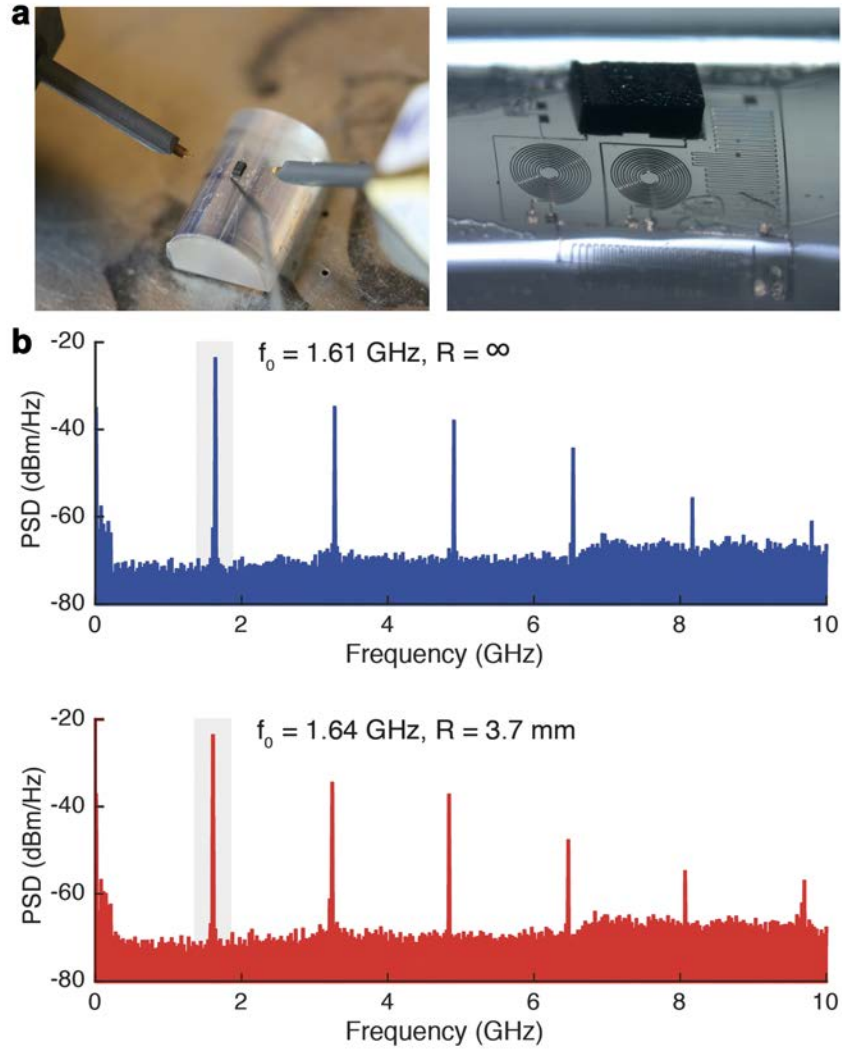


Figure S15. Colpitts oscillator on flexible polyimide substrate. a) Optical images. b) Measured PSDs of the oscillator at flat and bent (Bending radius, $R = 3.7 \text{ mm}$) conditions.

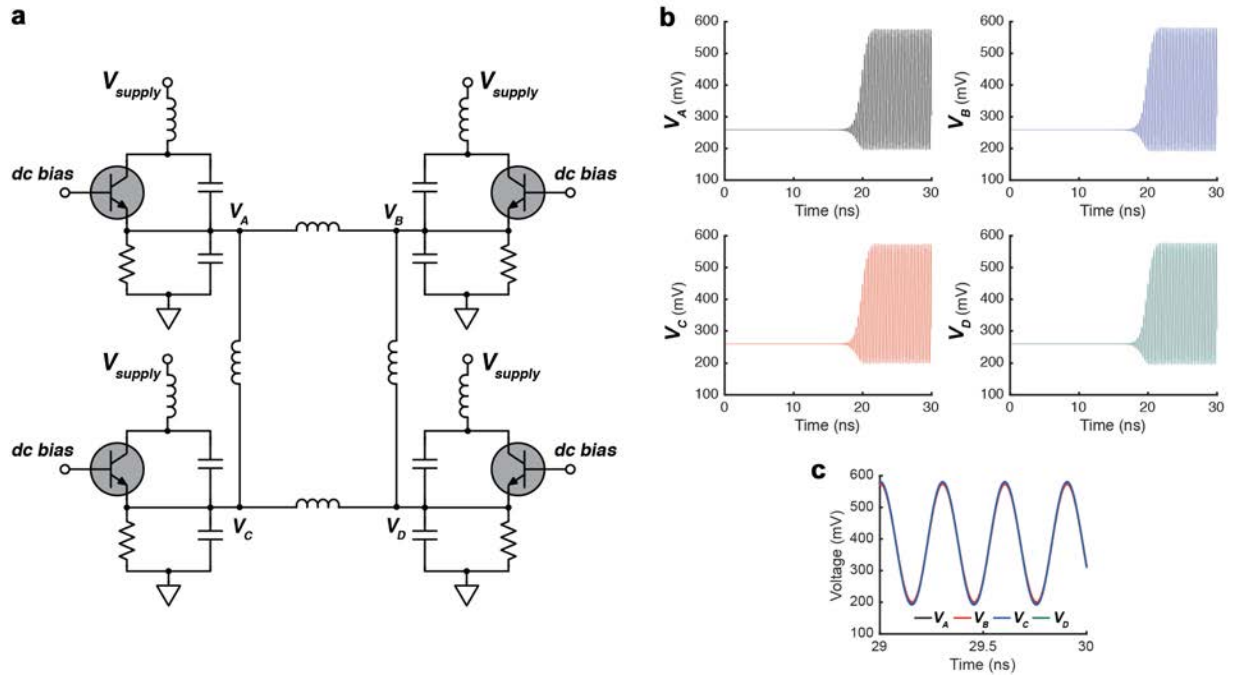


Figure S16. Simulation of injection-locked Colpitts oscillator array. a) Circuit schematic. b) Time-domain simulation of the four coupled oscillators showing the oscillation startup as well as its settlement into steady state. c) Overlay of the time-domain signals of (b) shows ideal frequency synchronization.

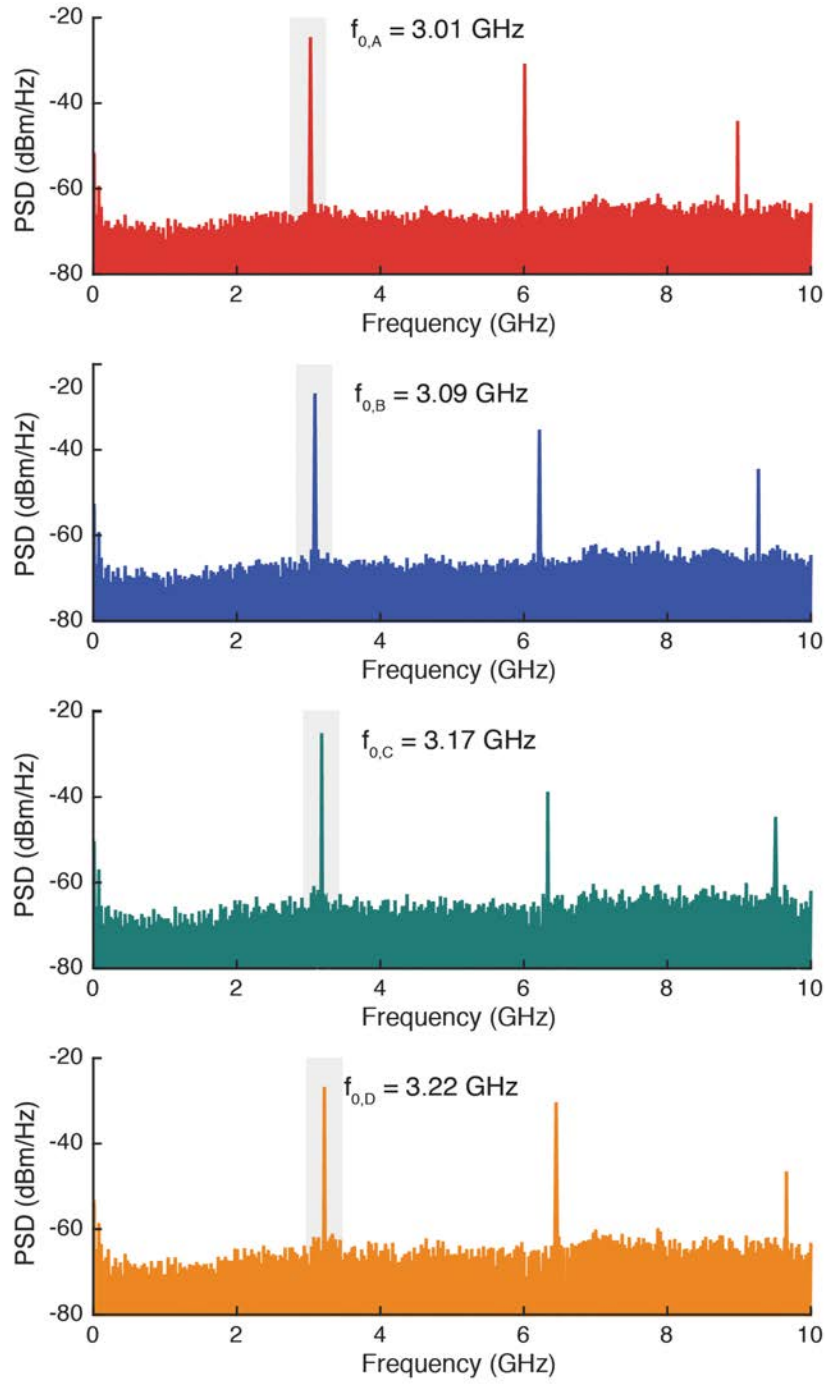


Figure S17. Uncoupled oscillations. Before the 4 Colpitts oscillators of Figure 2d are coupled and synchronized via injection locking, they oscillate at 4 different measured frequencies.

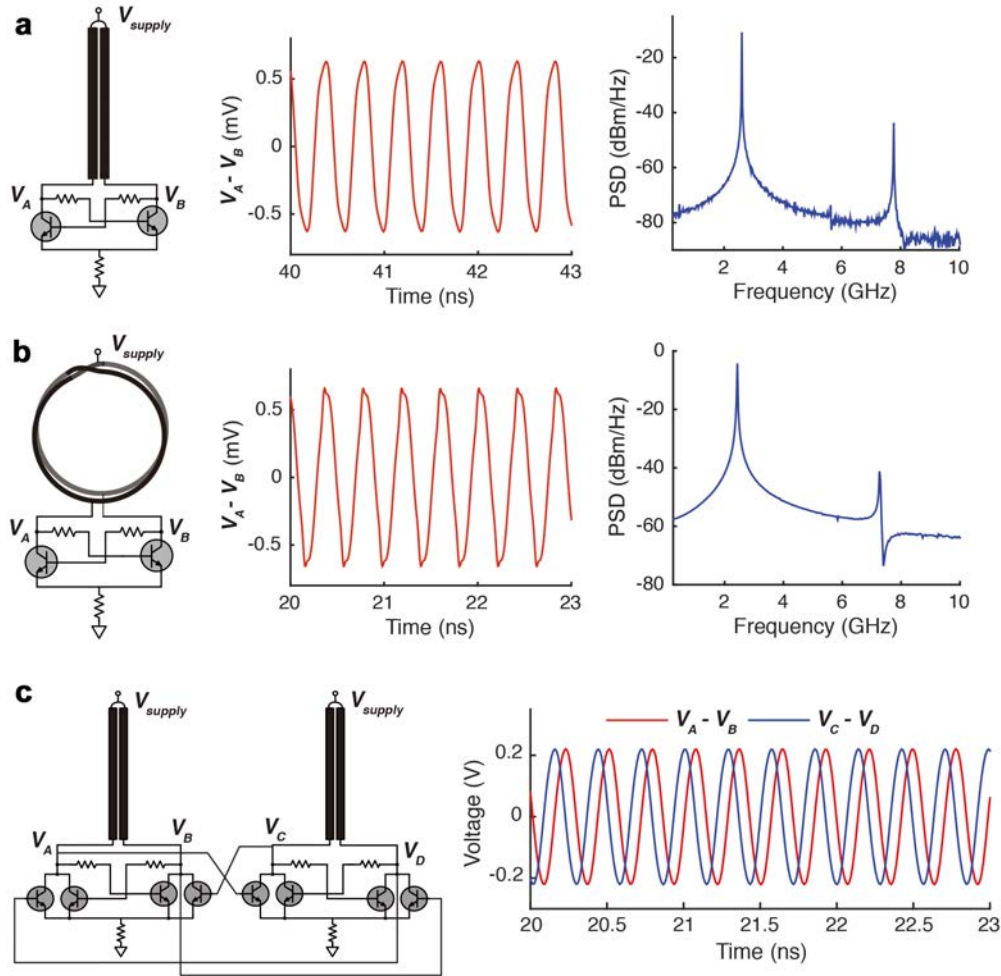


Figure S18. Simulation of oscillators with wave-based resonators. a) Simulated differential voltage output of the oscillator based on the CPS SWR in time and frequency domains. Due to the differential nature of the signal, the even harmonics are completely suppressed in this ideal simulation. b) Simulated differential voltage output of the CPS Möbius ring oscillator in time and frequency domains. Once again, due to the differential nature of the signal, the even harmonics are completely suppressed. c) Time-domain simulation of the ideal quadrature oscillators based on the CPS SWRs shows the exact 90° phase difference.

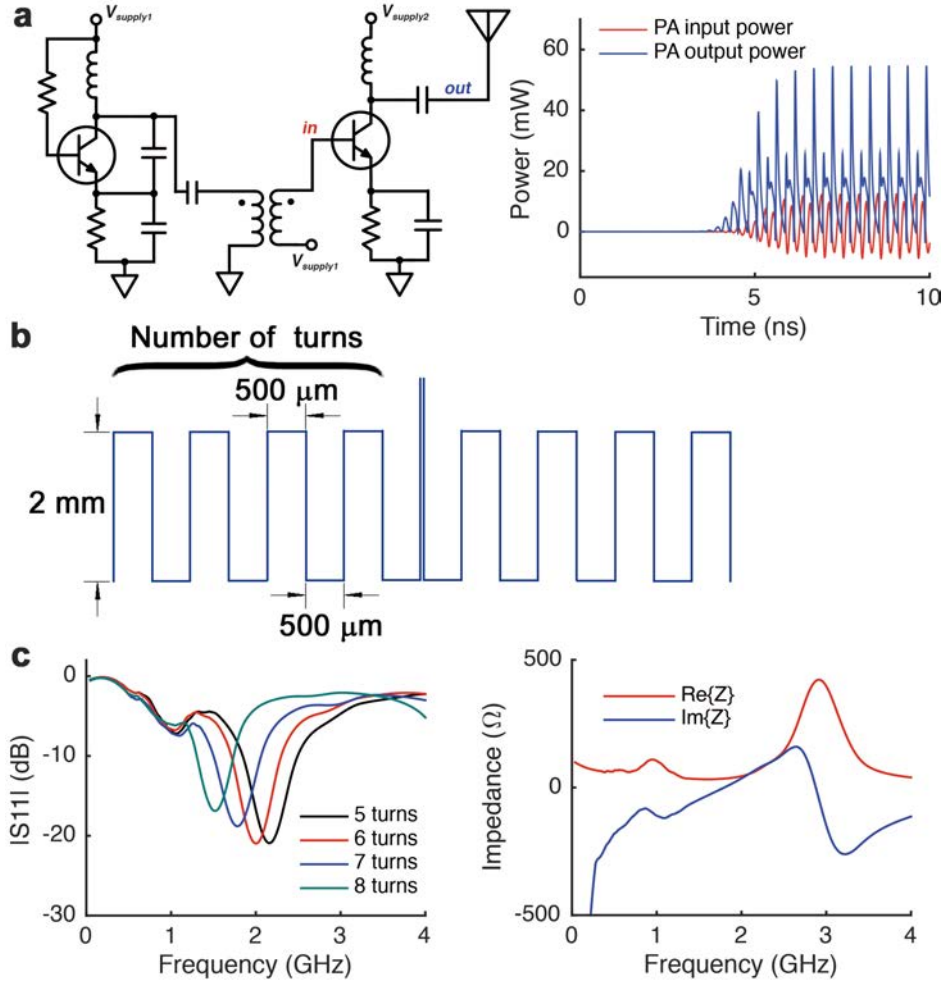


Figure S19. Wireless transmitter design and antenna measurements. a) Simulation of the RF transmitter of Figure 4. The power amplifier is loaded with the antenna’s measured s -parameter. Red and blue traces on the right are the power amplifier’s input and output power, respectively, and the average power gain is 12.7 dB. b) Schematic of the dipole antenna of Figure 4. It consists of two symmetrical arms, with each arm featuring a meandered silver trace. By tuning the overall arm length (for instance, by changing the number of turns), the antenna can be designed to resonate at the design frequency of 1.8 GHz. We choose a 7-turn (per arm) design for optimum radiation at 1.8 GHz. c) (Left) Magnitude of the measured s_{11} of antennas with varying number of turns. For the 7-turn antenna, the s_{11} magnitude becomes minimum at ca. 1.8 GHz, showing the optimum resonant radiation at the frequency. (Right) Input impedance of the 7-turn antenna extracted from the measured s_{11} . Its imaginary part is nulled at ca. 1.8 GHz, showing once again the resonant radiation at the frequency. The radiation resistance at 1.8 GHz is 35 Ω , the real part of the input impedance.

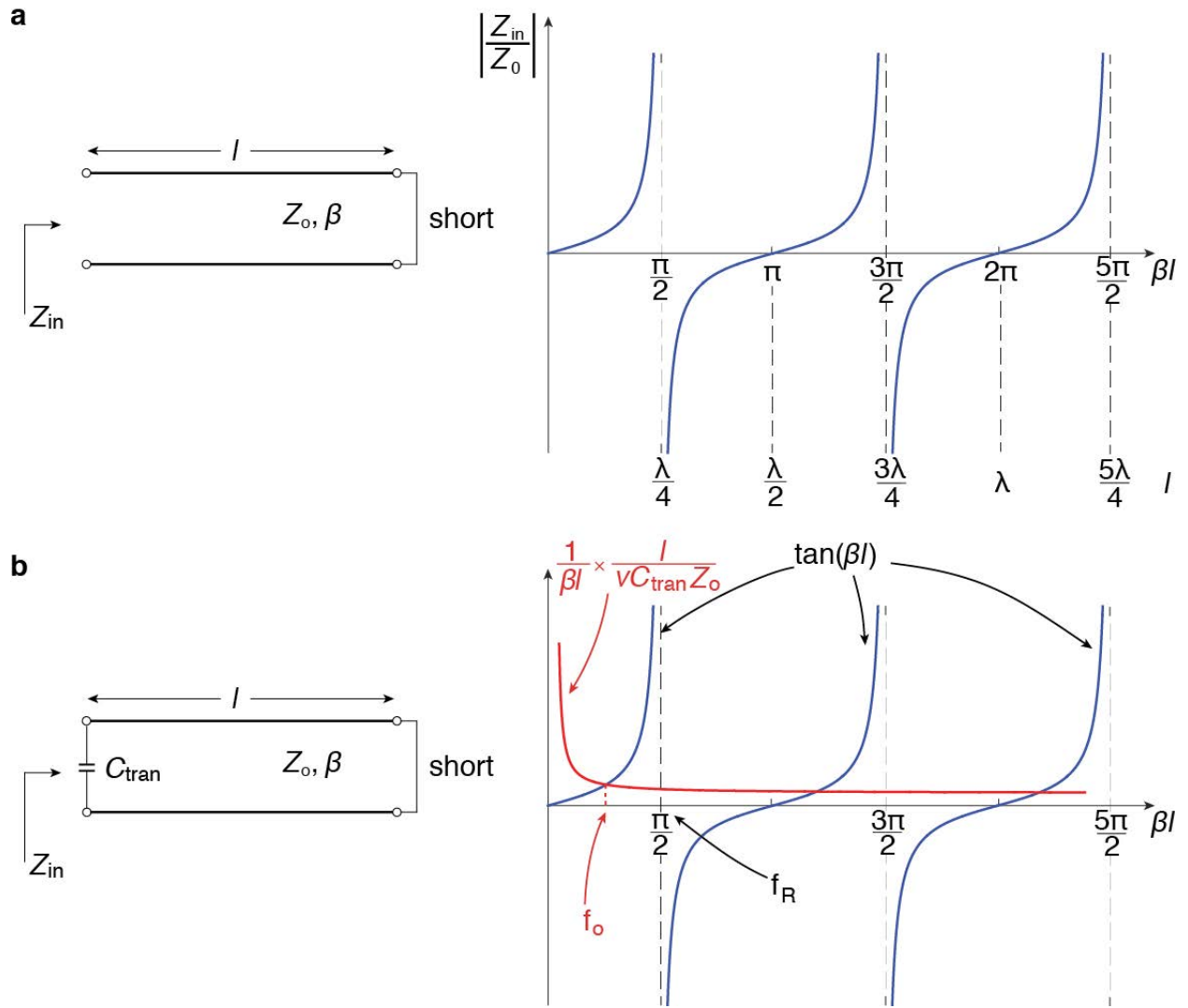
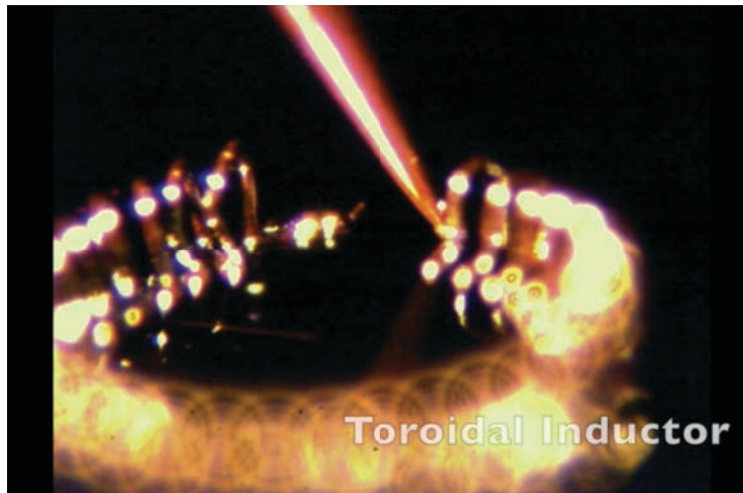
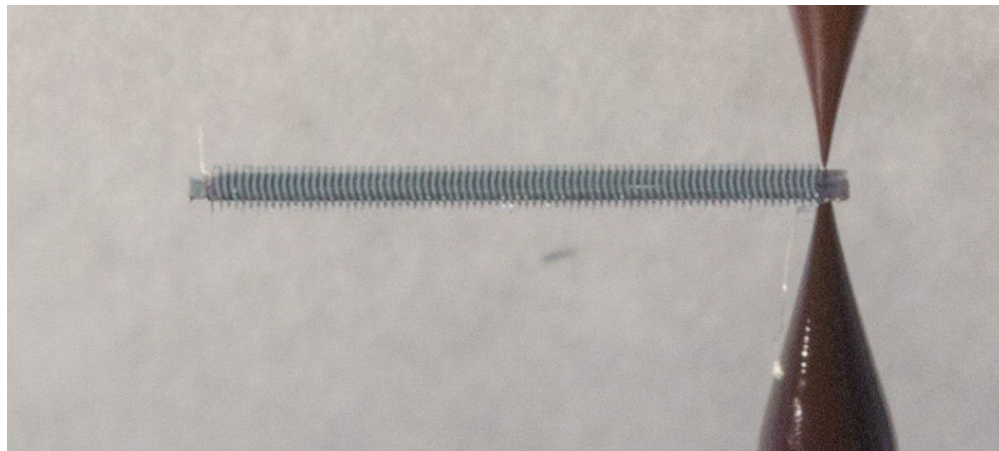


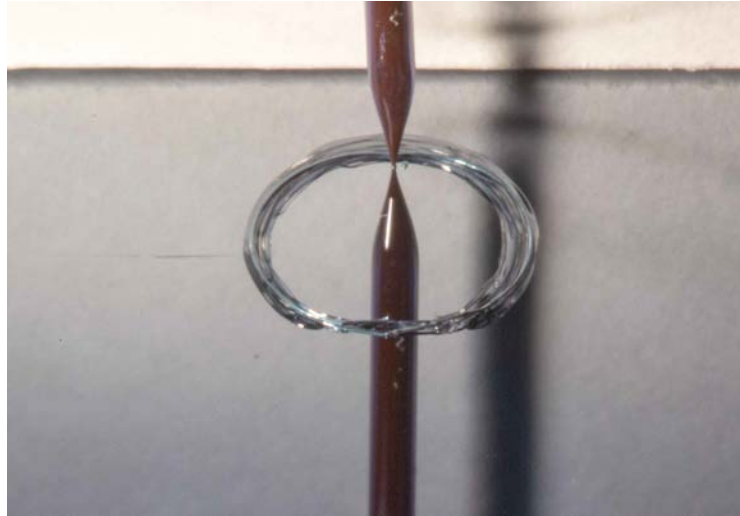
Figure S20. a) CPS SWR Z_{in} as a function of βl . b) Determination of f_0 when the CPS SWR is loaded with parasitic capacitance.



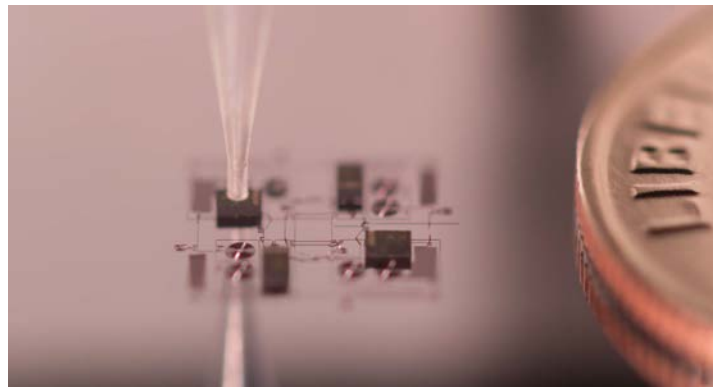
Movie S1. Direct writing of the silver nanoparticle ink through a 10- μm nozzle to create a planar spiral inductor, a toroidal inductor, a parallel plate capacitor, and a 3:1 transformer, captured using a high-resolution camera (uEye, IDS Imaging Development Systems) mounted on the 3D printing system (8 \times playback for the planar inductor and capacitor, 40 \times playback for the toroidal inductor and transformer).



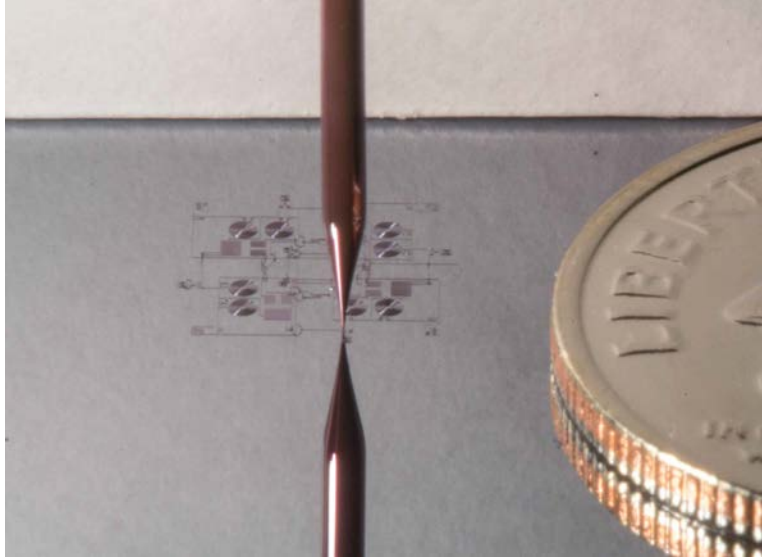
Movie S2. Direct writing of the silver nanoparticle ink through a 10- μm nozzle to create of an FMS-loaded CPS SWR, which shows the sequential printing of the CPS, a polystyrene sacrificial layer, and FMS features. The video is captured using a stationary camera (Canon EOS 5D) (30 \times playback). [Note: The removal of the polystyrene layer is not shown].



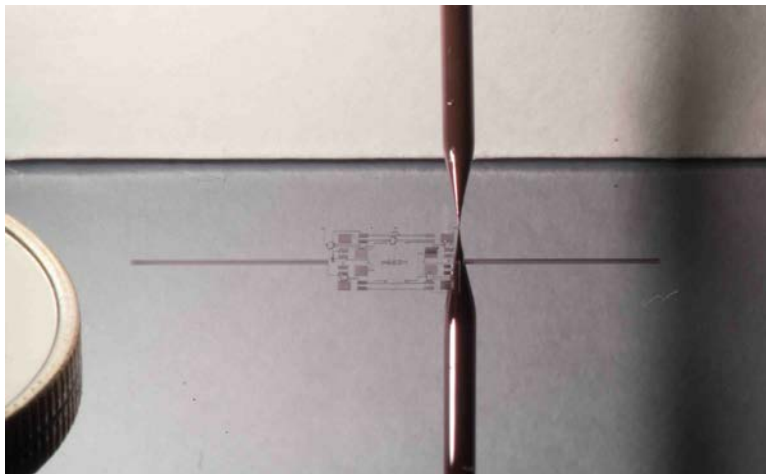
Movie S3. Direct writing of the silver nanoparticle ink through a 50- μm nozzle to create a Möbius CPS ring (5 mm in diameter), which shows the sequential printing of the bottom ring, a polystyrene sacrificial layer, and the top ring. The video is captured by the Canon EOS 5D camera (30 \times playback). [The removal of the polystyrene layer is not shown.]



Movie S4. Placement of surface mount transistors using an empty 200- μm plastic nozzle to apply a negative pressure, as captured by the Canon EOS 5D camera (30 \times playback). [Note: While this video illustrates transistor placement using this approach, the circuit has not been tested for its connectivity. The actual pick and place process used to create an operational circuit is more involved due to manual orientation of the device.]



Movie S5. Direct writing of the silver nanoparticle ink through a 10- μm nozzle to create the passive elements of an array of four injection-locked Colpitts oscillators, which is carried out prior to placement of surface mount transistors, captured by the Canon EOS 5D camera (40 \times playback).



Movie S6. Direct writing of the silver nanoparticle ink through a 10- μm nozzle to create the passive elements of injection-locked quadrature oscillators, which is carried out prior to the placement of surface mount transistors, captured by the Canon EOS 5D camera (90 \times playback).